

# VIBRATION CHARACTERISTICS OF ROTATING FUNCTIONALLY GRADED POROUS BEAMS REINFORCED BY GRAPHENE PLATELETS

Chu Thanh Binh<sup>a</sup>, Tran Huu Quoc<sup>a,\*</sup>, Duong Thanh Huan<sup>b</sup>, Ho Thi Hien<sup>a</sup>

<sup>a</sup>*Faculty of Building and Industrial Construction, National University of Civil Engineering, 55 Giai Phong road, Hai Ba Trung district, Hanoi, Vietnam*

<sup>b</sup>*Vietnam National University of Agriculture, Trau Quy town, Gia Lam district, Hanoi, Vietnam*

## **Article history:**

*Received 07/08/2021, Revised 28/08/2021, Accepted 31/08/2021*

---

## **Abstract**

This work aims to study the vibration characteristics of the rotating functionally graded porous beam reinforced by graphene platelets. The beam is mounted and rotated around a hub with a constant velocity. The material properties vary along the thickness direction with two types of porosity distributions and two dispersion patterns of graphene platelet. The equations of motion based on the Timoshenko beam theory are obtained and solved using the Chebyshev-Ritz method. The effects of the parameters such as hub radius, rotating speed, weight fraction, porosity distribution, porosity coefficient, and dispersion model are presented. The present method results are also compared with numerical results available in the literature.

*Keywords:* rotating Timoshenko beam; vibration; functionally graded material; porous material; graphene platelets.

[https://doi.org/10.31814/stce.huce\(nuce\)2021-15\(4\)-03](https://doi.org/10.31814/stce.huce(nuce)2021-15(4)-03) © 2021 Hanoi University of Civil Engineering (HUCE)

---

## **1. Introduction**

Many engineering structures can be modeled by rotating beams, such as turbine blades, propellers, wind turbine blades, helicopter rotor blades, and robotic manipulators. Thus, modeling and analysis of rotating beams have attracted interest from scientists. The earliest study on vibration characteristics of the rotating beam was reported by Southwell and Gough [1]. After that, many related works [2–10] in a variety of methods were published.

Functionally graded material (FGM) is a new type of composite material. This material is superior to conventional composite and has been applied in various fields, including automotive, shipbuilding, aerospace, etc. The FGM material has also been investigated via experimental and theoretical methods. Many studies have been developed to investigate the static and free vibration analysis of FGM beams [11–15]. Recently, functionally graded porous material (FGP), one type of FGM, have been attracted remarkable the attention of researchers. In addition, to enhance the performance of these materials, the reinforcement by graphene platelets (GPLs) into the FGP materials as additives have been studied. Several studies about the influence of graphene platelets (GPL) on the mechanical behaviors of functionally graded porous reinforced by graphene platelets (FGP-GPL) structures under several

---

\*Corresponding author. *E-mail address:* [quocth@nuce.edu.vn](mailto:quocth@nuce.edu.vn) (Quoc, T. H.)

different conditions have been conducted in the last few years [16–20]. However, modeling and analysis of the FGP-GPL beam remain limited. Using Ritz method associated with the Timoshenko beam theory, Kitipornchai *et al.* [13] studied the buckling and vibrations behaviors of FG-PGRC beams with some types of porosity distribution. They also extended their studies to analyze the stability and post-buckling of FGP-GPL beams by the Galerkin method [21] and the third-order refined beam model [22]. In Ref. [22, 23], Barati and Zenkour presented the post-buckling of the FGP-GPL beam with geometrical imperfection.

It is accomplished from the literature that the vibration characteristics of the rotating FGP-GPL beams have not been reported in the literature, and it is studied in this paper. The FGP-GPL materials can be instituted by combining two types of porosity distributions and two types of graphene platelets dispersion patterns distributed along with the thickness of beams. Various numerical investigations are conducted to examine the influence of related parameters such as hub radius, rotating speed, porosity distribution, porosity coefficient, GPL weight fraction, and GPL dispersion patterns.

## 2. Theoretical formulations

### 2.1. Description of the model

Consider an FGP-GPL Timoshenko beam as shown in Fig. 1. The beam has length  $L$ , width  $b$ , and height  $h$ . One edge of the beam is clamped to a rigid hub of radius  $R$ , and the other edge is free. The hub rotates about its longitudinal axis at a constant velocity  $\Omega$ . The coordinate system  $Oxyz$  with the origin of the coordinate system located at the center of the clamped edge is used.

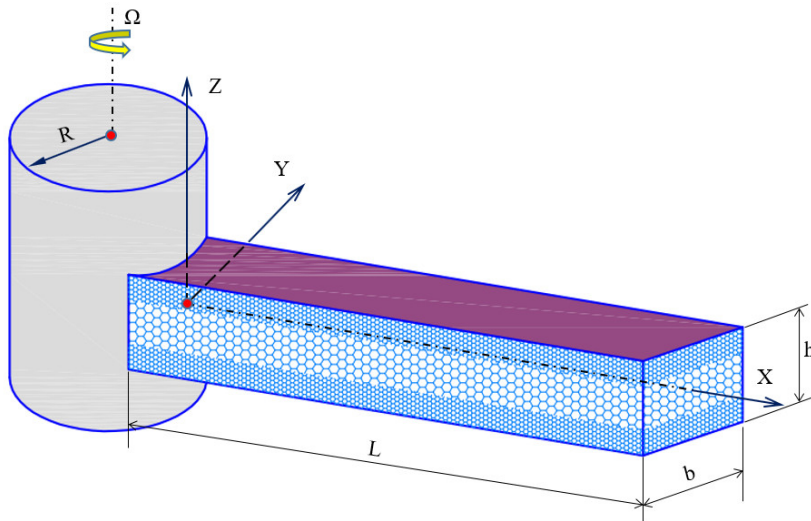


Figure 1. Rotating FGP-GPL Timoshenko beam

### 2.2. Material properties of FGP-GPL beams

In this study, two types of porosity distributions (PD), which are symmetric distribution (PDS) and asymmetric distribution (PDA), and two types of GPL dispersion patterns, which are symmetric dispersion patterns (GPLS) and uniform dispersion patterns (GPLU), are considered (Fig. 2).

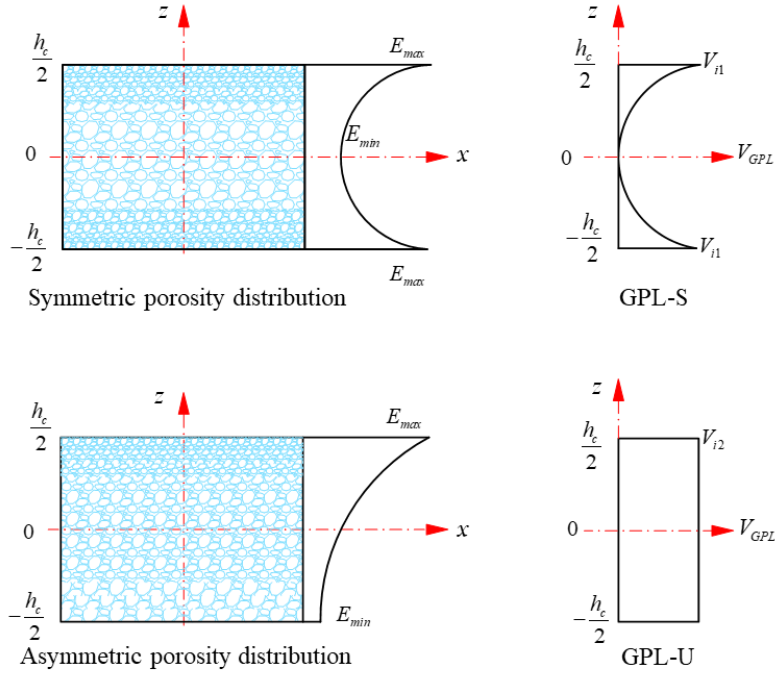


Figure 2. Porosity distributions and GPL dispersion patterns

The material properties of FGP-GPL material are explicitly formulated as

$$\begin{cases} E(z) = E_1 [1 - e_0\chi(z)] \\ G(z) = G_1 [1 - e_0\chi(z)] \\ \rho(z) = \rho_1 [1 - e_m\chi(z)] \end{cases} \quad (1)$$

where

$$\chi(z) = \begin{cases} \cos(\pi z/h_c) & \text{for PDS} \\ \cos(\pi z/h_c + \pi/4) & \text{for PDA} \end{cases} \quad \left(-\frac{h_c}{2} \leq z \leq \frac{h_c}{2}\right) \quad (2)$$

in which  $E_1$  and  $\rho_1$  are the highest values of effective Young's modulus and mass density. Meanwhile, the porosity coefficient  $e_0$  can be defined as

$$e_0 = 1 - \frac{E_{\min}}{E_{\max}}, \quad (0 \leq e_0 \leq 1) \quad (3)$$

In Eq. (3),  $E_{\max}$  and  $E_{\min}$  are the maximum and minimum elastic modulus values for the FGP core layer without GPL reinforcement. According to the Gaussian random field (GRF) model [24], the mechanical properties can be given as:

$$\frac{E(z)}{E_1} = \left(\frac{\rho(z)/\rho_1 + 0.121}{1.121}\right)^{2.3} \quad \text{for} \quad \left(0.15 < \frac{\rho(z)}{\rho_1} < 1\right) \quad (4)$$

Then, the mass coefficient  $e_m$  is given as

$$e_m = \frac{1.121 \left(1 - \sqrt[2.3]{1 - e_0\chi(z)}\right)}{\chi(z)} \quad (5)$$

The Poisson's ratio  $\nu(z)$  can be determined by [25]:

$$\nu(z) = 0.221\ell + \nu_1(0.342\ell^2 - 1.21\ell + 1) \quad (6)$$

where  $\nu_1$  is the Poisson's ratio of non-porous and  $\ell$  can be defined as

$$\ell = 1.121\left(1 - \sqrt[2.3]{1 - e_0\chi(z)}\right) \quad (7)$$

The GPL volume fraction is expressed as

$$V_{GPL}(z) = \begin{cases} V_{is} [1 - \cos(\pi z/h_c)] & \text{for GPLS} \\ V_{iu} & \text{for GPLU} \end{cases} \quad (8)$$

where  $V_s$  and  $V_u$  represent the peak values of GPL volume fraction, which can be calculated by [26]:

$$\frac{\Lambda_{GPL}\rho_m}{\Lambda_{GPL}\rho_m + \rho_{GPL}(1 - \Lambda_{GPL})} \times \int_{-h_c/2}^{h_c/2} [1 - e_m\chi(z)] dz = \int_{-h_c/2}^{h_c/2} V_{GPL}(z) [1 - e_m\chi(z)] dz \quad (9)$$

The highest value of elastic modulus of the non-porous metal matrix reinforced by GPLs is achieved using the Halpin-Tsai micromechanics model as [27, 28]:

$$E_1 = \frac{3}{8} \left( \frac{\xi_L \eta_L V_{GPL}}{1 - \eta_L V_{GPL}} \right) E_m + \frac{5}{8} \left( \frac{1 + \xi_W \eta_W V_{GPL}}{1 - \eta_W V_{GPL}} \right) E_m \quad (10)$$

in which

$$\xi_L = \frac{2l_{GPL}}{t_{GPL}}; \quad \xi_W = \frac{2w_{GPL}}{t_{GPL}}; \quad \eta_L = \frac{(E_{GPL}/E_m) - 1}{(E_{GPL}/E_m) + \xi_L}; \quad \eta_W = \frac{(E_{GPL}/E_m) - 1}{(E_{GPL}/E_m) + \xi_W} \quad (11)$$

where  $l_{GPL}$ ,  $w_{GPL}$ ,  $t_{GPL}$ ,  $E_m$ , and  $E_{GPL}$  are the average GPL length, GPL width, GPL thickness, elastic modulus metal matrix, and the elastic modulus of GPL material, respectively. The Poisson's ratio and the mass density of the metal matrix reinforced GPLs are defined by [28]:

$$\nu_1 = \nu_{GPL}V_{GPL} + \nu_m V_m; \quad \rho_1 = \rho_{GPL}V_{GPL} + \rho_m V_m \quad (12)$$

Finally, the relationship of GPL volume fraction  $V_{GPL}$  and metal matrix  $V_m$  can be expressed as,  $V_{GPL} + V_m = 1$ .

### 2.3. Energy functional

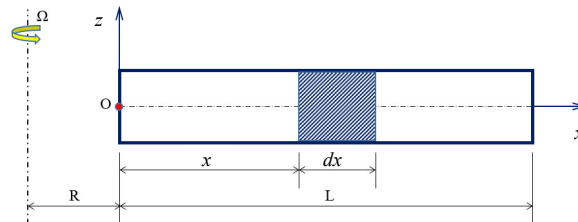


Figure 3. The rotating beam element

Consider the rotating beam element shows in Fig. 3.

According to the the assumption of Hodges and Rutkowski [29] and neglecting terms which are greater than  $\varepsilon^2$  strain-displacement, the strain field of the Timoshenko beam can be given as,

$$\varepsilon(x) = u'_0 - z\theta' + \frac{(w')^2}{2} \tag{13a}$$

$$\gamma_{xz}(x) = w' - \theta \tag{13b}$$

$$\gamma_{xy}(x) = 0 \tag{13c}$$

Accordingly, the strain energy of the beam can be expressed as

$$U = \frac{1}{2} \int_V (E(z) \varepsilon^2 + G(z) \gamma_{xz}^2) dV = \frac{1}{2} \int_0^L \int_A E(z) \left[ u'_0 - z\theta' + \frac{(w')^2}{2} \right]^2 dx dA + \frac{1}{2} \int_0^L \int_A G(z) (w' - \theta)^2 dx dA \tag{14}$$

in which, the strain  $\varepsilon_0(x)$  is related to the axial displacement  $u_0(x)$  by

$$\varepsilon_0(x) = u'_0(x) = \frac{T(x)}{A_1} \tag{15}$$

where  $A_1 = \int_{-h/2}^{h/2} E(z) b dz$  and  $T(x)$  is the centrifugal force and  $x$  is distant from the origin to cross-section and given as

$$T(x) = \int_x^L A_2 \Omega^2 (R + x) dx \tag{16}$$

in which  $A_2 = \int_{-h/2}^{h/2} \rho(z) b dz$ .

According to equations (14)–(16), the strain energy of the rotating beam can be obtained as:

$$U = \frac{1}{2} \int_0^L \{ A_3 (\theta')^2 + T (w')^2 + k A_4 (w' - \theta)^2 \} dx \tag{17}$$

where  $A_3 = \int_{-h/2}^{h/2} E(z) z^2 b dz$ ,  $A_4 = \int_{-h/2}^{h/2} G(z) b dz$ , and  $k = 5/6$  is the shear correction factor.

For the rotating Timoshenko beam, the kinetic energy is given as,

$$V = \frac{1}{2} \int_A \int_0^L (V_x^2 + V_y^2 + V_z^2) \rho dA dx \tag{18}$$

where  $V_x, V_y, V_z$  are velocities at a point along the  $x, y,$  and  $z$  directions and given as:

$$V_x = -z\dot{\theta}; \quad V_y = -\Omega(x + u_0 - z\theta); \quad V_z = \dot{w} \tag{19}$$

substituting Eq. (19) into Eq. (18) gives

$$\begin{aligned}
 V = & \frac{1}{2} \int_A \int_0^L \rho \Omega^2 (x + u_0)^2 dx dA + \frac{1}{2} \int_A \int_0^L \rho \Omega^2 z^2 \theta^2 dx dA \\
 & - \frac{1}{2} \int_A \int_0^L 2\rho \Omega^2 z \theta (x + u_0)^2 dx dA + \frac{1}{2} \int_A \int_0^L \rho z^2 \dot{\theta}^2 dx dA + \frac{1}{2} \int_A \int_0^L \rho \dot{w}^2 dx dA
 \end{aligned} \tag{20}$$

In Eq. (20), the first integral is constant, and the third equals zero. Therefore, the kinetic energy can be written as

$$V = \frac{1}{2} \left[ \int_0^L A_5 (\Omega^2 \theta^2 + \dot{\theta}^2) dx + \int_0^L A_6 \dot{w}^2 dx \right] \tag{21}$$

where  $A_5 = \int_{-h/2}^{h/2} \rho(z) z^2 b dz$ ,  $A_6 = \int_{-h/2}^{h/2} \rho(z) b dz$ .

Finally, the energy functional  $\Pi$  for beam vibration problem is obtained as

$$\Pi = U - V \tag{22}$$

#### 2.4. Solution procedure

In this work, the Chebyshev polynomial series is used to approximate the displacements of the beam:

$$w(\xi) = F_w(\xi) \sum_{i=1}^{\infty} \bar{w}_i P_i(\xi); \quad \theta(\xi) = F_\theta(\xi) \sum_{i=1}^{\infty} \bar{\theta}_i P_i(\xi) \tag{23}$$

where  $\xi = \frac{x}{L}$  is dimensionless coordinate,  $P_i(\xi)$  ( $i = 1, 2, 3, \dots$ ) is the  $i$ th one-dimensional Chebyshev polynomial, which can be written as follows:

$$P_i(\xi) = \cos[(i - 1) \arccos(2\xi - 1)], \quad \xi \in [0, 1] \tag{24}$$

in which  $F_w(\xi)$  and  $F_\theta(\xi)$  are boundary functions, which are shown in Table 1.

Table 1. Boundary functions  $F_w(\xi)$  and  $F_\theta(\xi)$  for various boundary conditions

Boundary functions	Boundary conditions					
	C-F	C-P	C-C	P-F	P-P	P-C
$F_w(\xi)$	$\xi$	$\xi(1 - \xi)$	$\xi(1 - \xi)$	$\xi$	$\xi(1 - \xi)$	$\xi(1 - \xi)$
$F_\theta(\xi)$	$\xi$	$\xi$	$\xi(1 - \xi)$	1	1	$1 - \xi$

Note: Symbols C, F, and P denote the clamped, free, and pinned boundary conditions, respectively.

Eq. (23) into Eq. (17) and Eq. (21) and minimizing the functional  $\Pi$  about the coefficients of the admissible functions, namely,

$$\frac{\partial \Pi}{\partial \bar{w}} = 0, \quad \frac{\partial \Pi}{\partial \bar{\theta}} = 0, \quad (i = 1, 2, \dots, n) \tag{25}$$

The governing equation can be obtained in matrix form:

$$\left( \begin{bmatrix} [K^{ww}] & [K^{w\theta}] \\ [K^{\theta w}] & [K^{\theta\theta}] \end{bmatrix} - \omega^2 \begin{bmatrix} [M^{ww}] & 0 \\ 0 & [M^{\theta\theta}] \end{bmatrix} \right) \begin{Bmatrix} \{\bar{w}\} \\ \{\bar{\theta}\} \end{Bmatrix} = \begin{Bmatrix} \{0\} \\ \{0\} \end{Bmatrix} \quad (26)$$

The frequency of the FGP-GPL beam will be obtained by solving the eigenvalue Eq. (26).

### 3. Numerical results and discussion

The effects of different factors such as rotational speed, hud radius, porosity coefficient, porosity distributions, weight fraction, and GPLs patterns on the frequency of the FGP-GPL beam are investigated in this section. The mechanical properties of the constituent material are considered as:

$$\begin{cases} E_m = 130 \text{ GPa}, \rho_m = 8960 \text{ kg/m}^3, \nu_m = 0.34 \\ E_{GPL} = 1.01 \text{ TPa}, \rho_{GPL} = 1062.5 \text{ kg/m}^3, \nu_m = 0.186, w_{GPL} = 1.5 \mu\text{m}, l_{GPL} = 2.5 \mu\text{m}, t_{GPL} = 1.5 \text{ nm} \end{cases}$$

For convenient, dimensionless parameters are introduced as follows:

$$\bar{\omega} = \omega \sqrt{\frac{\rho_m AL^4}{E_m I}}; \quad \bar{\Omega} = \Omega \sqrt{\frac{\rho_m AL^4}{E_m I}}; \quad \delta = \frac{R}{L}$$

where  $\omega$  is the natural frequency of the beam,  $\Omega$  is the angular velocity.

#### 3.1. Convergence study

At first, a convergence study is conducted to obtain the number of shape functions in Ritz's expansion to reach a reasonable accuracy. For this purpose, the first five dimensionless natural frequencies of the rotating FGP-GPL beam are obtained for many shape functions ( $N_m$ ). The convergence characteristics of the numerical results are shown in Table 2.

Table 2. The first five nondimensional frequencies  $\bar{\omega}$  of an FGP-GPL beam (PDA, GPLU,  $e_0 = 0.2$ ,  $\Lambda_{GPL} = 1\%$ ,  $L = 1 \text{ m}$ ,  $h = 0.2 \text{ m}$ ,  $b = 0.2 \text{ m}$ ,  $\delta = 0$ ,  $\bar{\Omega} = 10$ )

$N_m$	Mode number				
	Mode 1	Mode 2	Mode 3	Mode 4	Mode 5
3	12.835	41.916	105.934	300.826	337.597
4	12.786	38.266	92.506	174.960	304.811
5	12.779	38.251	80.103	155.131	247.282
6	12.779	38.240	79.649	130.634	224.146
7	12.779	38.238	79.449	128.990	186.372
8	12.779	38.238	79.440	128.032	182.889
9	12.779	38.238	79.440	127.979	180.232
10	12.779	38.238	79.440	127.969	180.028

From Table 2, it is seen that with the increase in the number of shape functions ( $N_m$ ), the frequencies converge rapidly and monotonically from above to stable values. The difference between the two number of shape functions  $N_m = 9$  and  $N_m = 10$  is not significant. Therefore, from a practical point of view, the number of shape functions  $N_m = 10$  is used in the rest of this study.

### 3.2. Comparative study

The first comparison is conducted to compare the obtained dimensionless frequency  $\bar{\omega}$  of rotating isotropic beam with those reported by Wang and Wereley [30]. The comparison in Table 3 shows that the present results agree well with the benchmark solution. The maximum discrepancy is less than 2.88%.

Table 3. Comparison dimensionless frequency  $\bar{\omega}$  of rotating isotropic beam ( $\delta = 0$ )

Dimensionless Frequencies	Dimensionless rotational speed $\bar{\Omega}$					
	$\bar{\Omega} = 0$			$\bar{\Omega} = 12$		
	[29]	Present	Error (%)	[29]	Present	Error (%)
$\bar{\omega}_1$	3.516	3.513	0.09	13.170	13.160	0.08
$\bar{\omega}_2$	22.034	21.930	0.47	37.603	37.480	0.33
$\bar{\omega}_3$	61.697	60.980	1.16	79.614	78.910	0.88
$\bar{\omega}_4$	120.902	118.300	2.15	140.534	138.100	1.73
$\bar{\omega}_5$	199.860	194.100	2.88	220.536	214.800	2.60

In the following example, the first three dimensionless frequencies  $\hat{\omega} = \frac{\omega L^2}{h} \sqrt{\frac{\rho_m}{E_m}}$  of the rotating FGM beam are investigated. In this specific example, the dimensionless parameters are defined:  $\eta^2 = \frac{B_1 L^4 \Omega^2}{A_2}$ ,  $B_1 = \int_{-\frac{h}{2}}^{\frac{h}{2}} \rho(z) dz$ ,  $A_2 = \int_{-\frac{h}{2}}^{\frac{h}{2}} E(z) z^2 dz$ . The present results are compared with those reported by Ebrahimi and Mokhtari [31] in Table 4.

Table 4. Comparison dimensionless frequency  $\hat{\omega}$  of rotating FGM beam ( $L/h = 20, h/b = 1, R/L = 0, \eta = 8$ )

$p$	Method	Dimensionless frequencies		
		$\hat{\omega}_1$	$\hat{\omega}_2$	$\hat{\omega}_3$
0	[31]	5.131	16.493	38.011
	Present	5.129	16.487	37.999
1	[31]	4.305	13.840	31.895
	Present	4.304	13.835	31.886
5	[31]	3.864	12.402	28.476
	Present	3.863	12.398	28.467
10	[31]	3.567	11.447	26.275
	Present	3.566	11.443	26.265

The excellent agreement observed for this particular problem, in addition to the previous examples, should confirm the accuracy of the present model.

### 3.3. Parametric study

#### a. Influence of the porosity distributions and the GPL dispersion patterns

The porosity distributions and GPL dispersion patterns (GPLD) are the most important parameters of the structure made of FGP-GPL. Thus, the influence of PD and GPLD should be investigated. Considering the beam with length  $L = 1$  m, cross-sectional dimension  $b \times h = 0.2 \times 0.2$  m is made of FGP-GPL material with component material properties as described above. The results of the dimensionless vibration frequencies  $\bar{\omega}$  of the beam with different input parameters are presented in Table 5. As shown in Table 5, the beams with PDS pore distribution model combined with GPLS reinforcement have the highest frequency, followed by the combination between PDS and GPLU, and PDA and GPLS models, while the combination between PDA and GPLU has the smallest vibration frequency. Table 5 also shows that when the GPL ratio increases, the vibration frequency of the beam increases in all cases of the material model considered, while the rise of the porosity coefficient will cause the beam to vibrate at a lower frequency. The reason is that when the mass of GPL increases, the stiffness of the beam will increase, while the increase of the porosity coefficient will make the stiffness of the beam decrease.

Table 5. Dimensionless frequency  $\bar{\omega}$  of rotating FGP-GPL beam ( $L = 1$  m,  $b = h = 0.2$  m,  $\bar{\Omega} = 10$ ,  $\delta = 0.2$ )

PD	$e_0$	GPLS			GPLU		
		$\Lambda_{GPL} (\%)$					
		0.2	0.5	1	0.2	0.5	1
PDS	0.0	12.331	12.516	12.806	12.284	12.404	12.591
	0.1	12.319	12.503	12.792	12.273	12.392	12.579
	0.3	12.298	12.481	12.766	12.252	12.371	12.558
	0.5	12.282	12.464	12.748	12.238	12.357	12.546
PDA	0.0	12.331	12.516	12.806	12.284	12.404	12.591
	0.1	12.306	12.488	12.772	12.261	12.378	12.562
	0.3	12.257	12.431	12.703	12.214	12.326	12.504
	0.5	12.209	12.376	12.636	12.168	12.276	12.447

#### b. Influence of porosity coefficient

The influence of the porosity coefficient  $e_0$  on the natural frequency of the FGP-GPL rotary beam is investigated and presented in Fig. 4. The results show that when the porosity coefficient increases, the vibration frequency of the FGP-GPL beam will decrease. However, the beam's vibration frequency will decrease sharply with the PDA porosity distribution pattern, while the PDS distribution pattern will make the beam's vibration frequency decrease slightly. This observation shows that the porosity distribution plays a significant role in the force-resistance capacity of the FGP-GPL beam.

#### c. Influence of the nanofiller weight fraction $\Lambda_{GPL}$

In this section, the influence of the GPL ratio on the vibration frequency of the FGP-GPL beam is investigated and presented in Fig. 5. In this example, the FGP-GPL beam has two porosity distribution patterns and two types of GPL reinforcement were investigated with the porosity coefficient  $e_0 = 0.5$ . The results show that, with a small amount of GPL added, the stiffness of the beam increases

significantly. It can be concluded that the GPL ratio plays a vital role in increasing the stiffness of the beam. Fig. 5 also shows that the GPLS reinforcement gives a higher frequency result than the GPLU reinforcement, which leads to the conclusion that good reinforcement will provide better efficiency in GPL utilization. Specifically, with the same amount of reinforced GPL, the combination of PDS and GPLS will give the maximum beam stiffness.

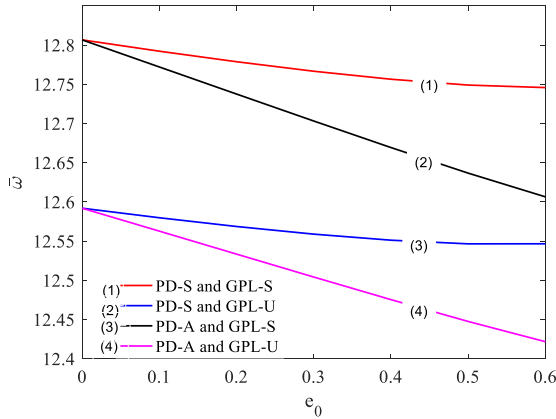


Figure 4. Dimensionless natural frequencies  $\bar{\omega}$  of the FGP-GPL beam versus porosity coefficient  $e_0$  ( $L = 1$  m,  $b = h = 0.2$  m,  $\Lambda_{GPL} = 1\%$ ,  $\bar{\Omega} = 10$ ,  $\delta = 0.2$ )

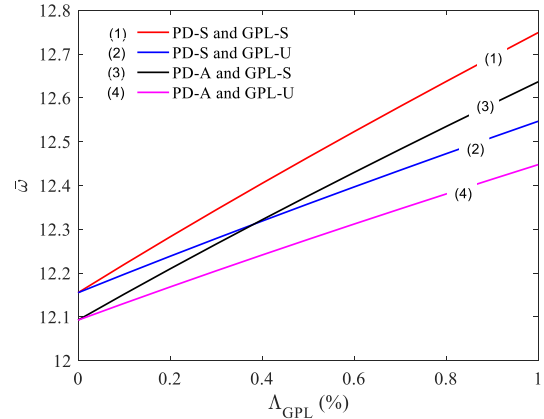


Figure 5. Dimensionless natural frequencies  $\bar{\omega}$  of the FG-PGRC beam versus nanofiller weight fraction  $\Delta_{GPL}$  ( $L = 1$  m,  $b = h = 0.2$  m,  $e_0 = 0.5$ ,  $\bar{\Omega} = 10$ ,  $\delta = 0.2$ )

d. Influence of the angular velocity

The different behaviors between the rotating and non-rotating beams come from the effect of centrifugal force due to the rotational velocity. Therefore, angular velocity  $\bar{\Omega}$  is the important parameter that should be investigated. A rotating FGP-GPL beam with length  $L=1$ m, rectangular cross-section  $b \times h = 0.2 \times 0.2$  m are considered. The hub has a radius  $R = 0.2$  m and rotates with constant angular velocity. The obtained dimensionless frequencies  $\bar{\omega}$  are listed in Table 6. It is observed that the

Table 6. Dimensionless frequencies  $\bar{\omega}$  of the FGP-GPL beam for different angular velocity  $\bar{\Omega}$  ( $L = 1$  m,  $b = h = 0.2$  m,  $e_0 = 0.5$ ,  $\Lambda = 1\%$ ,  $\delta = 0.5$ )

$\bar{\Omega}$	Material model			
	PDS, GPLS	PDS, GPLU	PDA, GPLS	PDA, GPLU
0.0	4.9125	4.4149	4.6111	4.1201
1.0	5.0576	4.5759	4.7658	4.2928
2.0	5.4688	5.0268	5.2013	4.7718
3.0	6.0896	5.6957	5.8519	5.4734
4.0	6.8596	6.5113	6.6507	6.3191
5.0	7.7306	7.4212	7.5466	7.2539
6.0	8.6689	8.3910	8.5055	8.2438
7.0	9.6520	9.3995	9.5054	9.2682
8.0	10.6654	10.4332	10.5325	10.3148
9.0	11.6998	11.4839	11.5781	11.3762
10.0	12.7489	12.5465	12.6366	12.4475

frequencies of the beam increase as the rotational speed parameter  $\bar{\Omega}$  increases. This observation can come from the fact that the centrifugal force increases by increasing the rotational speed, thus causing the beam's higher bending stiffness and higher frequencies. The results, again, indicate that the combination between PDS and GPLS has the highest value of frequencies  $\bar{\omega}$ , while the combination between PDA and GPLU has the lowest value of frequencies  $\bar{\omega}$ .

Variations of the first three dimensionless natural frequencies  $\bar{\omega}$  of a rotating FGP-GPL beam (PDS, GPLS) versus the dimensionless angular velocity  $\bar{\Omega}$  are tabulated in Fig. 6. It can be seen that the natural frequency increase due to the centrifugal stiffening is much evident for lower modes than the higher ones.

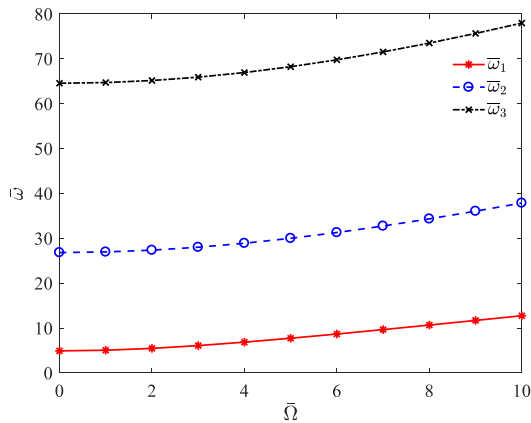


Figure 6. Dimensionless frequencies  $\bar{\omega}$  of the FGP-GPL beam versus dimensionless angular velocity  $\bar{\Omega}$  ( $L = 1$  m,  $b = h = 0.2$  m,  $e_0 = 0.5$ ,  $\Lambda = 1\%$ , PDS, GPLS,  $\delta = 0.5$ )

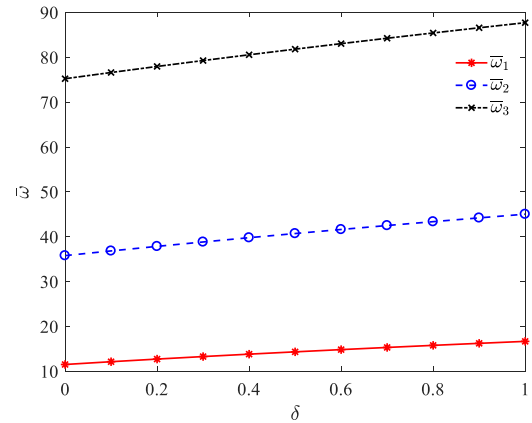


Figure 7. Dimensionless natural frequencies  $\bar{\omega}$  of the FGP-GPL beam versus the  $\delta$  ratio ( $L = 1$  m,  $b = h = 0.2$  m,  $e_0 = 0.5$ ,  $\Lambda = 1\%$ , PDS, GPLS,  $\bar{\Omega} = 10$ )

e. Influence of the  $\delta = R/L$  ratio

The vibrational characteristics of a rotating FGP-GPL beam are affected by many physical and geometrical parameters such as material properties, angular velocity, thickness, length, etc. The in-

Table 7. Dimensionless frequencies  $\bar{\omega}$  of the FGP-GPL beam for different  $\delta$  ( $L = 1$  m,  $b = h = 0.2$  m,  $e_0 = 0.5$ ,  $\Lambda = 1\%$ ,  $\bar{\Omega} = 10$ )

$\delta$	Material model			
	PDS, GPLS	PDS, GPLU	PDA, GPLS	PDA, GPLU
0.0	11.5439	11.3223	11.4196	11.2117
0.1	12.1619	11.9506	12.0441	11.8464
0.2	12.7489	12.5465	12.6366	12.4475
0.3	13.3091	13.1143	13.2017	13.0200
0.4	13.8459	13.6577	13.7427	13.5675
0.5	14.3619	14.1796	14.2626	14.0930
0.6	14.8594	14.6824	14.7635	14.5991
0.7	15.3402	15.1680	15.2474	15.0876
0.8	15.8060	15.6381	15.7160	15.5603
0.9	16.2580	16.0187	16.1707	16.0187
1.0	16.6974	16.5370	16.6125	16.4640

fluence of material properties was investigated in the above example. In this example, the effect of the ratio  $\delta = R/L$  is considered. The results are shown in Table 7 and tabulated in Fig. 7. It can be observed that the hub radius has a significant effect on the centrifugal force and therefore also significantly affects the bending stiffness and frequency of the beam.

#### 4. Conclusions

In summary, this paper shows our contribution to developing the Timoshenko beam theory and the Chebyshev-Ritz method for the vibration characteristics of the rotating FGP-GPL beams. The calculated results are compared with the ones in the literature with excellent agreement. The natural frequencies are calculated, and related graphics are plotted. The effects of the porosity distributions and the GPL dispersion patterns, porosity coefficient, nanofiller weight fraction, angular velocity, hub radius, and rotational speed are investigated. The numerical results indicate that the natural frequencies increase with the nanofiller weight fraction, rotational speed, and hub radius while decreasing with the porosity coefficient. The combination between PDS and GPLS has the highest stiffness while PDA and GPLU have the lowest one.

#### References

- [1] Southwell, R., Gough, F. (1921). *The free transverse vibration of airscrew blades*. British A. R. C. Reports and Memoranda, UK, No. 766.
- [2] Bhat, R. B. (1986). [Transverse vibrations of a rotating uniform cantilever beam with tip mass as predicted by using beam characteristic orthogonal polynomials in the Rayleigh-Ritz method](#). *Journal of Sound and Vibration*, 105(2):199–210.
- [3] Yoo, H. H., Shin, S. H. (1998). [Vibration analysis of rotating cantilever beams](#). *Journal of Sound and Vibration*, 212(5):807–828.
- [4] Mao, Q. (2014). [Free vibrations of spinning beams under nonclassical boundary conditions using adomian modified decomposition method](#). *International Journal of Structural Stability and Dynamics*, 14(07): 1450027.
- [5] Yokoyama, T. (1988). [Free vibration characteristics of rotating Timoshenko beams](#). *International Journal of Mechanical Sciences*, 30(10):743–755.
- [6] Lin, S. C., Hsiao, K. M. (2001). [Vibration analysis of a rotating Timoshenko beam](#). *Journal of Sound and Vibration*, 240(2):303–322.
- [7] Banerjee, J. R., Sobey, A. J. (2002). [Energy expressions for rotating tapered Timoshenko beams](#). *Journal of Sound and Vibration*, 254(4):818–822.
- [8] Yardimoglu, B. (2006). [Vibration analysis of rotating tapered Timoshenko beams by a new finite element model](#). *Shock and Vibration*, 13(2):117–126.
- [9] Kaya, M. O. (2006). [Free vibration analysis of a rotating Timoshenko beam by differential transform method](#). *Aircraft Engineering and Aerospace Technology*, 78(3):194–203.
- [10] Lee, B. K., Oh, S. J., Lee, T. E. (2013). [Free vibration of tapered Timoshenko beams by deformation decomposition](#). *International Journal of Structural Stability and Dynamics*, 13(02):1250057.
- [11] Tham, V. V., Tu, T. M. (2016). [Static and free vibration analysis of functionally graded beam using various shear deformation theories](#). *Journal of Science and Technology in Civil Engineering (STCE) - NUCE*, 10 (2):15–22.
- [12] Hung, D. X., Truong, H. Q. (2018). [Free vibration analysis of sandwich beams with FG porous core and FGM faces resting on Winkler elastic foundation by various shear deformation theories](#). *Journal of Science and Technology in Civil Engineering (STCE) - NUCE*, 12(3):23–33.
- [13] Kitipornchai, S., Chen, D., Yang, J. (2017). [Free vibration and elastic buckling of functionally graded porous beams reinforced by graphene platelets](#). *Materials & Design*, 116:656–665.

- [14] Chen, D., Yang, J., Kitipornchai, S. (2017). [Nonlinear vibration and postbuckling of functionally graded graphene reinforced porous nanocomposite beams](#). *Composites Science and Technology*, 142:235–245.
- [15] Phuong, N. T. B., Tu, T. M., Phuong, H. T., Long, N. V. (2019). [Bending analysis of functionally graded beam with porosities resting on elastic foundation based on neutral surface position](#). *Journal of Science and Technology in Civil Engineering (STCE) - NUCE*, 13(1):33–45.
- [16] Sahmani, S., Aghdam, M. M., Rabczuk, T. (2018). [Nonlinear bending of functionally graded porous micro/nano-beams reinforced with graphene platelets based upon nonlocal strain gradient theory](#). *Composite Structures*, 186:68–78.
- [17] Barati, M. R., Zenkour, A. M. (2018). [Vibration analysis of functionally graded graphene platelet reinforced cylindrical shells with different porosity distributions](#). *Mechanics of Advanced Materials and Structures*, 26(18):1580–1588.
- [18] Mirjavadi, S. S., Forsat, M., Hamouda, A. M. S., Barati, M. R. (2019). [Dynamic response of functionally graded graphene nanoplatelet reinforced shells with porosity distributions under transverse dynamic loads](#). *Materials Research Express*, 6(7):075045.
- [19] Anirudh, B., Ganapathi, M., Anant, C., Polit, O. (2019). [A comprehensive analysis of porous graphene-reinforced curved beams by finite element approach using higher-order structural theory: Bending, vibration and buckling](#). *Composite Structures*, 222:110899.
- [20] Li, Z., Zheng, J. (2020). [Structural failure performance of the encased functionally graded porous cylinder consolidated by graphene platelet under uniform radial loading](#). *Thin-Walled Structures*, 146:106454.
- [21] Bahaadini, R., Saidi, A. R. (2018). [On the stability of spinning thin-walled porous beams](#). *Thin-Walled Structures*, 132:604–615.
- [22] Barati, M. R., Zenkour, A. M. (2017). [Post-buckling analysis of refined shear deformable graphene platelet reinforced beams with porosities and geometrical imperfection](#). *Composite Structures*, 181:194–202.
- [23] Barati, M. R., Zenkour, A. M. (2018). [Analysis of postbuckling of graded porous GPL-reinforced beams with geometrical imperfection](#). *Mechanics of Advanced Materials and Structures*, 26(6):503–511.
- [24] Roberts, A. P., Garboczi, E. J. (2001). [Elastic moduli of model random three-dimensional closed-cell cellular solids](#). *Acta Materialia*, 49(2):189–197.
- [25] Roberts, A. P., Garboczi, E. J. (2002). [Computation of the linear elastic properties of random porous materials with a wide variety of microstructure](#). *Proceedings of the Royal Society of London. Series A: Mathematical, Physical and Engineering Sciences*, 458(2021):1033–1054.
- [26] Afdl, J. C. H., Kardos, J. L. (1976). [The Halpin-Tsai equations: A review](#). *Polymer Engineering and Science*, 16(5):344–352.
- [27] Tjong, S. C. (2013). [Recent progress in the development and properties of novel metal matrix nanocomposites reinforced with carbon nanotubes and graphene nanosheets](#). *Materials Science and Engineering: R: Reports*, 74(10):281–350.
- [28] Nakamura, T., Wang, T., Sampath, S. (2000). [Determination of properties of graded materials by inverse analysis and instrumented indentation](#). *Acta Materialia*, 48(17):4293–4306.
- [29] Hodges, D. H., Rutkowski, M. J. (1981). [Free-vibration analysis of rotating beams by a variable-order finite-element method](#). *AIAA Journal*, 19(11):1459–1466.
- [30] Wang, G., Wereley, N. M. (2004). [Free vibration analysis of rotating blades with uniform tapers](#). *AIAA Journal*, 42(12):2429–2437.
- [31] Ebrahimia, F., Mokhtaria, M. (2015). [Semi-analytical vibration characteristics of rotating Timoshenko beams made of functionally graded materials](#). *Latin American Journal of Solids and Structures*, 12(7): 1319–1339.